

Supplemental Material

Explosive-effusive-explosive: the role of magma ascent rates and paths in modulating caldera eruptions

Olivier Bernard^{1,2}, Weiran Li³, Fidel Costa^{1,2}, Steve Saunders⁴, Ima Itikarai⁴, Mikhail Sindang⁴, and Caroline Bouvet de Maisonneuve^{1,2}

¹Earth Observatory of Singapore, Nanyang Technological University, 50 Nanyang Ave, Block N2-01a-15, Singapore 639798

²Asian School of the Environment, Nanyang Technological University, 62 Nanyang Dr, Singapore 637459

³University of Cambridge, Department of Earth Sciences, Downing street, Cambridge CB2 3EQ, UK

⁴Rabaul Volcano Observatory, Papua-New-Guinea

MATERIALS AND METHODS

We studied samples representative of the sub-plinian, effusive, and vulcanian phases of the Rabaul 2006 eruption, which are pumices in a tephra fall deposit, fragments of a lava flow, and fragments of a ballistic cowpad bomb respectively (see details in Bernard and Bouvet de Maisonneuve, 2020). Samples were prepared into thin sections for analysis.

Analytical techniques

Single point electron microanalysis. Concentrations of major elements and volatiles (Cl and F) in apatite in the matrix and in clinopyroxene (Cpx) were obtained using a JEOL JXA 8530F field emission gun electron microprobe at the Facilities for Analysis, Characterisation, Testing and Simulation (FACTS), Nanyang Technological University (NTU). To obtain high precision halogen data in apatite to retrieve melt water content, we used a 15kV acceleration voltage, 10 nA beam current and a 10 μm diameter defocused beam. F, Cl and Na were measured first to minimize the migration of F and the loss of Na during the analysis. We used on peak counting times of 10s for Na, 20s for Ca and P, 40s for F, Fe and Mn, 60s for Cl, Si and Ce, 80s for S and, 100s for Mg. Backgrounds on both sides of the peak were measured for half of the peak time. We corrected and analyzed the data using the same standards and correction procedures as reported in Li (2019). The OH concentration was calculated based on apatite stoichiometry (Ketcham, 2015), assuming the anion site contains only F, Cl and OH. Relative errors in the determined concentration are <1% for Ca and P, $\sim 1\%$ for Cl and <2.5% for F. Overall, we analyzed 161 apatite in the three samples. Details on the number of single point analyses are reported in the table S1 and details of the analyses are reported in the spreadsheet, supplementary data analyses. We performed more than one point in some of the large crystals, and the maximum number of analysis on each crystal does not exceed four.

Sample	# of apatite analyzed (matrix / inclusion / total)	# of points collected (matrix / inclusion / total)
Sub-plinian pumice	16 / 24 / 40	24 / 32 / 56
Lava flow	23 / 34 / 57	48 / 42 / 90
Vulcanian cowpie bomb	32 / 32 / 64	38 / 35 / 73

Table S1: Numbers of apatite analyzed and single point analysis per type of sample. The detail of each of these analyses can be found in the attached spreadsheet “supplementary data analyses”.

For melt inclusions in the lava flow and the ballistic bomb we used a 15kV acceleration voltage, 6nA beam current and 10 μm diameter defocused beam. Na was measured first to avoid loss during analysis. We used on peak counting times of 10s for K, 20s for Na, Ca, Mn, Mg and Fe,

30s for Ti, 40s for Si and Al and 60s for Cl. We used the same standard correction as the one reported in Bouvet de Maisonneuve et al. (2015). Backgrounds on both sides of the peak were measured for half of the peak time. Melt inclusion data for the pumice were obtained from Bouvet de Maisonneuve et al., 2015. Melt inclusion data for the lava flow and the ballistic bomb are reported in the spreadsheet, supplementary data analyses.

Determination of zoning profiles for apatite. To probe the distribution of halogens in apatite, X-ray maps of Cl and F as well as cathodoluminescence images with a pixel size of 0.26 μm were acquired at the EPMA. We used an accelerating voltage of 15 kV, beam current of 25 nA, and dwell time of ~ 70 ms. Crystallographic orientation of apatite that show Cl/F zoning were determined with an EBSD (Electron back-scatter diffraction) detector mounted on a JEOL JSM-7800F Field Emission Scanning Electron Microscope (SEM), at the Asian School of the environment, NTU. The EBSD measurements were performed on thin section from which the carbon coating was removed to get an optimal diffraction pattern. We used a 20 kV acceleration voltage and a 12 nA beam current. Thin sections were tilted 70° from the horizontal to collect the diffracted electrons. Diffraction patterns were matched with a hexagonal structure of fluorapatite (Hughes et al., 1991).

Apatite traverses were collected using the same 15kV acceleration voltage and 10 nA beam current as single point analyses but we decrease the size of the beam to 1 μm in diameter to gain spatial resolution. Each compositional profile is acquired with a 1- μm spacing and at the smallest possible angle with the apatite c-axis (that was pre-determined by EBSD). Focus was given to the acquisition of F and Cl with a 60s and 100s counting time on peaks, respectively. Counting times on peaks was 20s for Na, P and Ca, 40s for Fe and Mn, 60s for Ce and 80s for Mg. Si and S were not acquired to decrease analysis time. We used the same background measurement, correction and data analysis procedures as for the single point analyses (Ketcham, 2015; Li, 2019). Relative errors in the determined concentrations are $<1\%$ for Ca and P, $\sim 1.5\%$ for Cl, and $\sim 2\%$ for F. All profiles used for modelling are reported in the spreadsheet, supplementary data analyses.

Calculation of melt water content from apatite

Single point analyses of crystal cores were used to calculate pre-eruptive melt water contents using the model of Li and Costa (2020). 218 single point analyses were used for calculation. We computed the exchange coefficient of OH-Cl between apatite and melt, using eq. 24 of Li and Costa (2020) and assuming a temperature of 975 $^\circ\text{C}$, as estimated from two-pyroxene thermometry (Bouvet de Maisonneuve et al., 2015) and the apatite saturation temperature (see below and Fig. S9). We use the same temperature for Cpx- and matrix-hosted apatite for ease of comparison. We then used the average Cl content (~ 4000 ppm) of Cpx-hosted melt inclusions that show no signs of post-entrapment modification (Bouvet de Maisonneuve et al., 2015) to calculate melt H_2O contents in equilibrium with Cpx- and matrix-hosted apatite. Details of the calculation steps can be found in paragraph 6 of Li and Costa (2020). The equation used to estimate the Cl-OH partition coefficient between melt and apatite is:

$$\ln \left(K_{D_{\text{OH-Cl}}^{\text{Ap-melt}}} \right) = -\frac{1}{RT} \times \left(\frac{72900(\pm 2900) - 34 \pm (0.3) \times T}{-1000 \times [5(\pm 2) \times (X_{\text{Cl}}^{\text{Ap}} - X_{\text{OH}}^{\text{Ap}}) - 10(\pm 8) \times X_{\text{F}}^{\text{Ap}}]} \right),$$

where $K_{D_{OH-Cl}^{Ap-melt}}$ is the exchange coefficient, T is temperature in kelvins, R is the gas constant, and X_{Cl}^{Ap} , X_{OH}^{Ap} and X_F^{Ap} are the mole fraction ratios of Cl, OH, and F respectively in apatite.

Kinetic/diffusion modelling of apatite zoning profiles

To estimate timescales of magma ascent we performed multi-component (F, Cl, OH) diffusion modelling of 16 profiles in zoned apatite crystals (Fig. 1, 3, Table 1), using the *ApTimer* diffusion model (Li et al., 2020a). Diffusivities were calculated using Arrhenius relations reported by Li et al. (2020a) at 925–975°C, based on two-pyroxene and plagioclase-liquid thermometry (Bouvet de Maisonneuve et al., 2015). Initial conditions used in our diffusion model are homogeneous F–Cl–OH profiles (assuming crystals are un-zoned before diffusion started) with F–Cl–OH concentrations equivalent to those measured for the cores of individual crystals. Boundary conditions were assumed to be equal to the F–Cl–OH compositions measured at positions closest to the crystal rims. We still fit the sub-plinian profiles with the model as they show a 2–3 μm wide concentration anomaly at the rim (see Fig. S2). However, we cannot be sure whether this anomaly is a measurement artifact due to the proximity with the matrix as it concerns only 1–2 points.

To be internally consistent the three profiles (Cl, F and OH) were always fitted at the same time, therefore, calculating a single value to assess the “quality of the fit” is not obvious. As such, we decided to report the normalized RMSD, which is a value that measures how far the diffusion is from the data (see definition below). Values of RMSD are reported in the attached spreadsheet “supplementary data analyses” as well as on the figures with the fitted profiles (Figures 3 of the manuscript and S1-S8 in this supplementary material).

Equation for calculating the normalized RMSD:

$$normalized\ RMSD = \frac{\sqrt{\frac{\sum_{i=1}^n (C_i^m - C_i^f)^2}{n}}}{mean(C^m)}$$

where n is the total number of data points in the profile where diffusion occurs (excluding the plateau part), i is the number of data point starting from one side of the profile (an integer between 1 and n), C_i^f and C_i^m are the fitted (modelled) and measured concentrations of a given element (in mole fractions in our model) at data point i . When the profile is perfectly fitted by the model, the $rmsd_n$ is equal to 0.

Calculation of Apatite saturation temperatures

We calculated apatite saturation temperature (AST) using the equation 1 in Piccoli and Candela (1994), which is based on melt composition only:

$$T = \frac{26,400 * C_{SiO_2} - 4,800}{12.4 * C_{SiO_2} - \ln(C_{P_2O_5}) - 3.97}$$

T is the apatite saturation temperature (in kelvins), and C_{SiO_2} and $C_{P_2O_5}$ are the weight fraction of SiO_2 and P_2O_5 in the melt in which the apatite begins to crystallize. We used melt inclusion and matrix glass data for calculation and obtained the same AST values of $962 \pm 28^\circ\text{C}$ (1-sigma standard deviation). Fig. S9 shows the results from 80 matrix glass analyses in the pumice (data from Bouvet de Maisonneuve et al., 2015).

Results of F–Cl–OH diffusion in apatite

We considered the fact that a compositional change in F–Cl–OH at the rim of apatite crystals may be related to either chemical diffusion, crystal growth, or both. Apatite crystals in the matrix of the lava show zoning profiles (parallel to the c-axis) over distances of $>40\ \mu\text{m}$. Cathodoluminescence images show a 2–10 μm wide bright zone at the rim (Fig. 3), which is likely related to zoning in REE and reflecting a late episode of growth (Cherniak, 2000). This bright zone is an order of magnitude shorter than the F–Cl–OH zoning and therefore, we considered that growth had limited impact on the profile of these elements. We also note that the absence of zoning in volatiles in apatite of the more explosive eruptions is consistent with a diffusive equilibration interpretation, rather than simply growth from the melt.

Diffusion modelling times are summarized in Table S2 below, while all zoning profiles with their best fit curves from diffusion modelling and the associated times are shown in Fig. S2–S5.

Eruptive Phase	Apatite	Traverse	Time (h) at T=925°C	Time (h) at T=950°C	Time (h) at T=975°C
Sub-plinian	1	1	28	20	12 (reverse zoning)
	6	1	23	13	8 (no real zoning)
	6	2	10	5.5	4 (no real zoning)
	11	1	13	8	5 (reverse zoning)
Effusive	4	1	5500 (229 d)	3000 (125 d)	1800 (75 d)
	4	2	4500 (188 d)	2500 (104 d)	1500 (63 d)
	6	1	1800 (75 d)	1000 (42 d)	650 (27 d)
	6	2	7500 (313 d)	4000 (167 d)	2200 (92 d)
	21	1	3600 (150 d)	2000 (83 d)	1200 (50 d)
	21	2	4200 (175 d)	2400 (100 d)	1300 (54 d)
Vulcanian	3	1	65	32	20
	3	2	49	24	15
	4	1	75	42	25
	4	2	85	50	28
	4 bis	1	26	16	9
	18	1	39	19	13

Table S2: F–Cl–OH modelling times in apatite. We reported diffusion time in hours for 3 different temperatures. Numbers in parenthesis for the effusive phase are in days. Comments on the sub-plinian apatite in parenthesis of no zoning indicate that the fit gave some diffusion time, however the resolution given by the profile measured at the EPMA was insufficient to consider the measured time as significant. The reverse zoning indicate that, F and OH zoning were reversed compared to all the other profiles seen in the other apatite which could be a marker of a different process.

SUPPLEMENTAL FIGURES

Figure S1–S8. F and Cl X-ray maps, Cathodoluminescence (CL) images, and Backscattered electron (BSE) images of apatites analyzed for diffusion modelling. The locations of compositional profiles used for diffusion modelling are marked with black and white arrows. Only the profiles modelled at 975°C are shown, however the modelled profile shapes are the same at 950 and 925°C, only the time (see Table S2) changes. There is barely any compositional change for both profiles in the sub-plinian apatite (S1-S2), which implies that the diffusion timescales obtained are likely to be overestimated. Error bars represent a 2% relative error on the measurements for Cl and F and 10% for OH. The $rmsd_n$ corresponds to the root mean square deviation calculation normalized to the mean of the measured data (the definition is explained in the the part on diffusion in this supplementary material).

Sub-plinian – Apatite 6

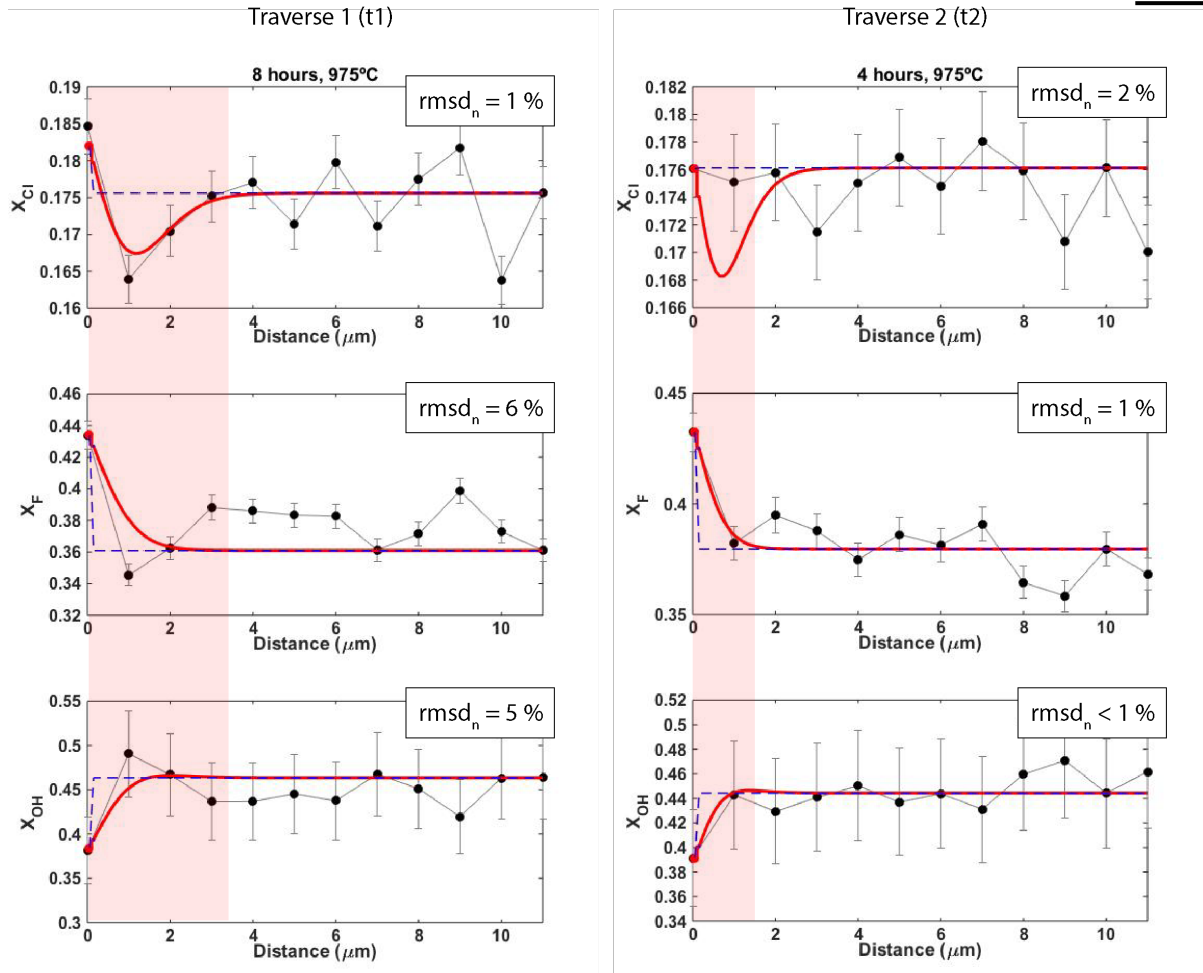
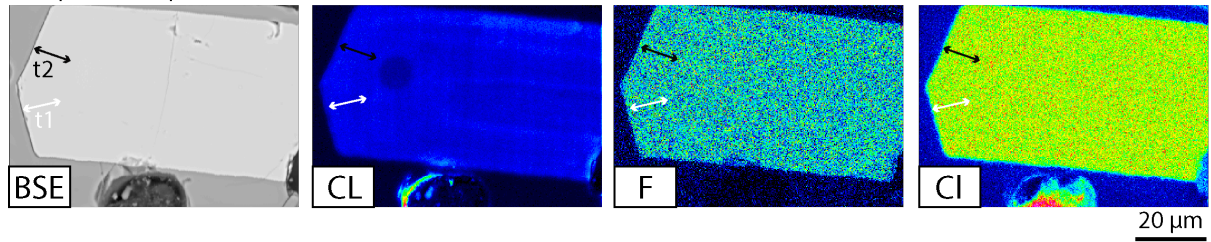
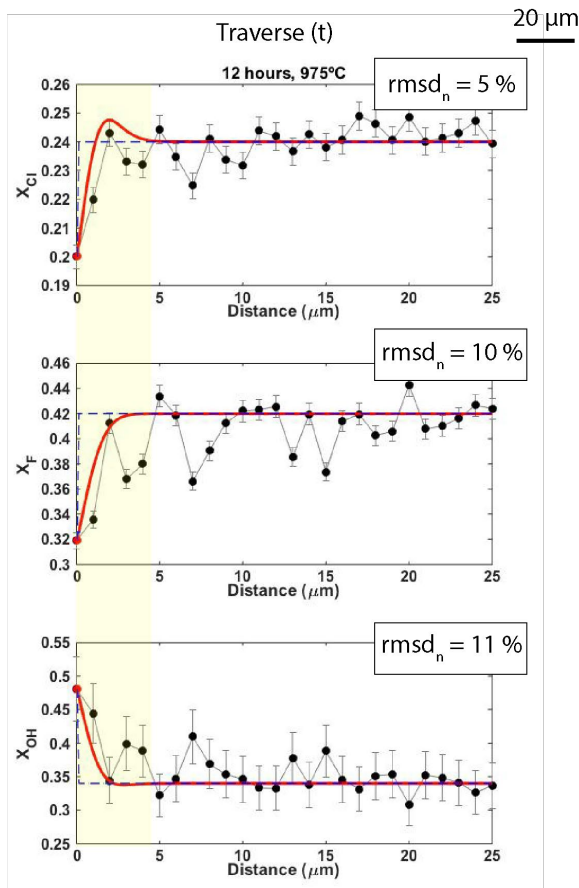
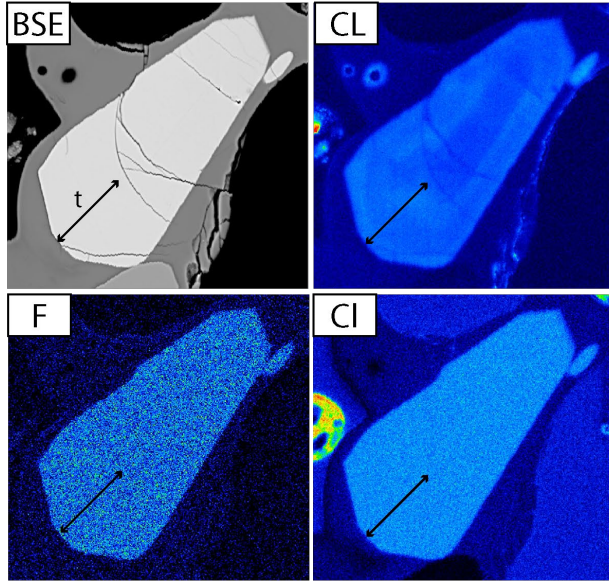


Figure S1. BSE, CL and F and CI X-ray maps of apatite 6 in the sub-plinian pumice and the associated measured profiles and best fit. The red zone corresponds to the points affected by diffusion.

Sub-plinian - Apatite 1



Sub-plinian - Apatite 11

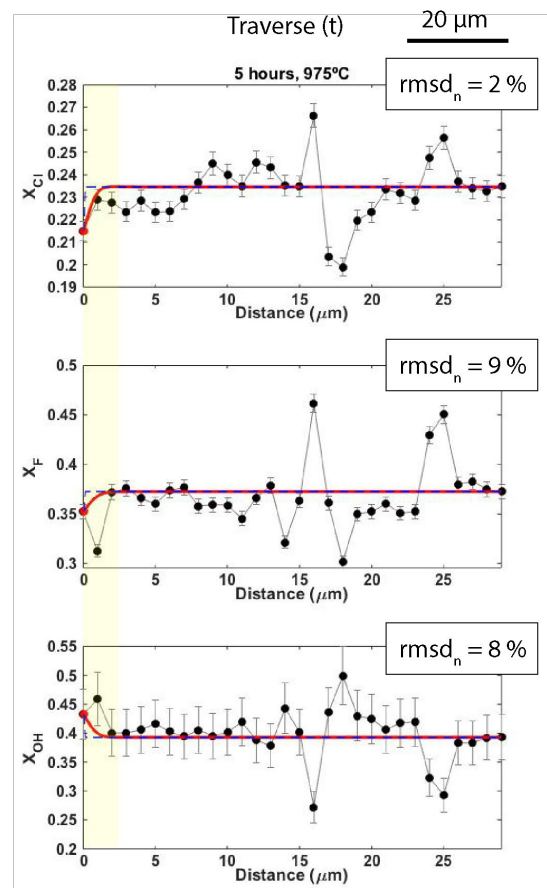
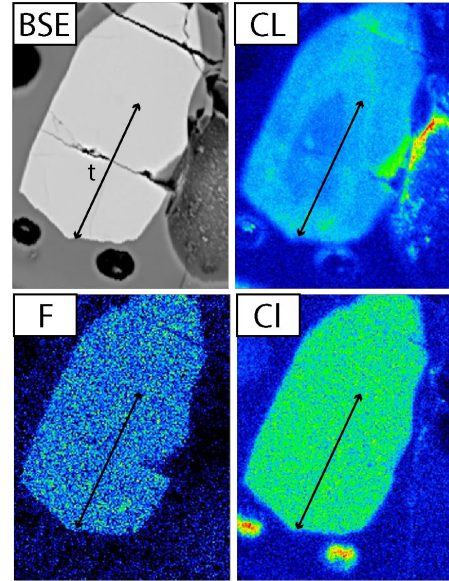


Figure S2. BSE, CL and F and CI X-ray maps of the sub-plinian apatite 1 and 11, and the associated measured profiles and best-fit models. The two apatite show reverse zoning in F and OH (especially apatite 1), which could link to an increase of volatile content in the melt right before eruption (highlighted by the yellow zone).

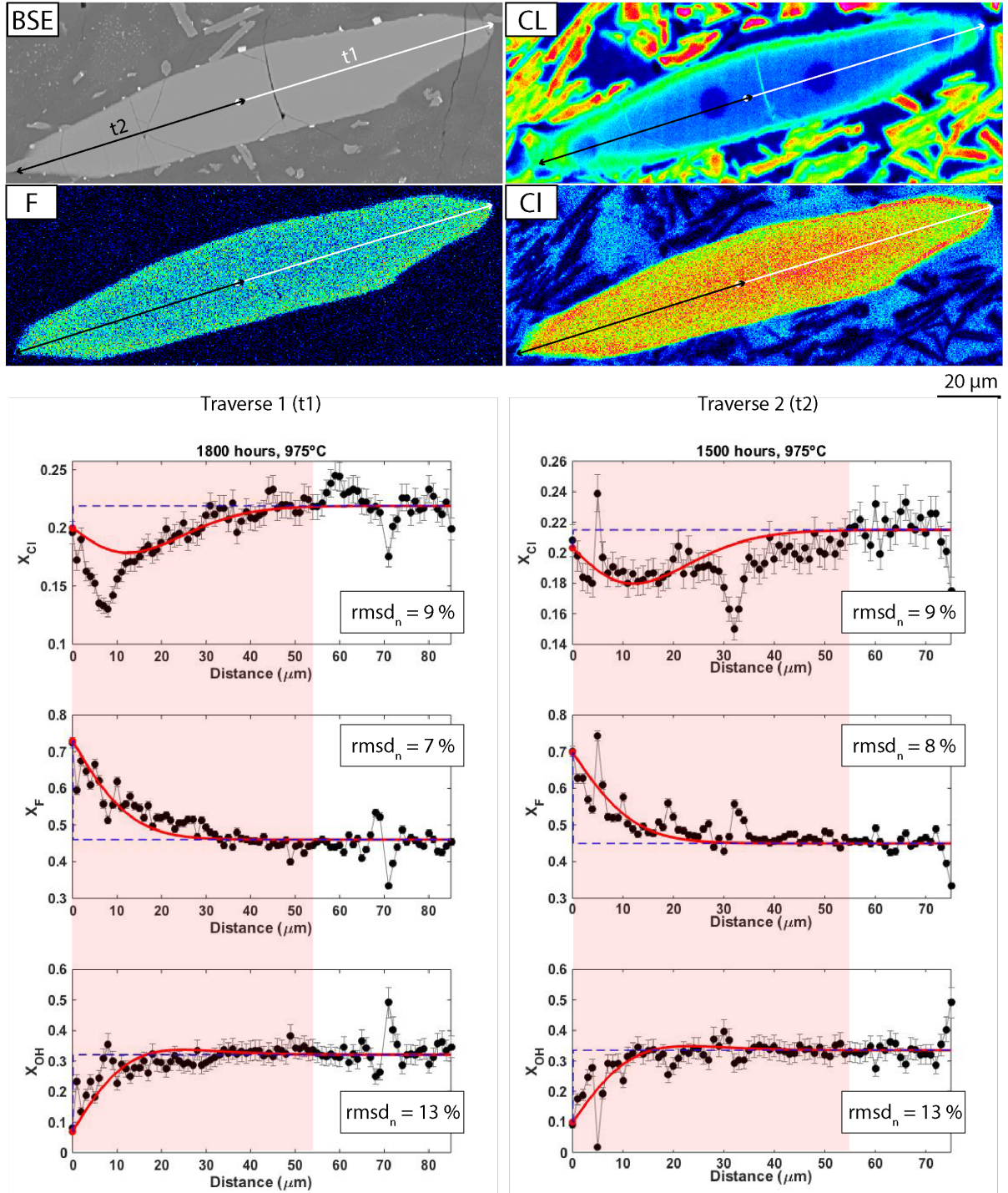


Figure S3. BSE, CL and F and Cl X-ray maps of apatite 4 in the lava flow and the associated measured profiles and best fit. The red zone corresponds to the points affected by diffusion.

Effusive – Apatite 6

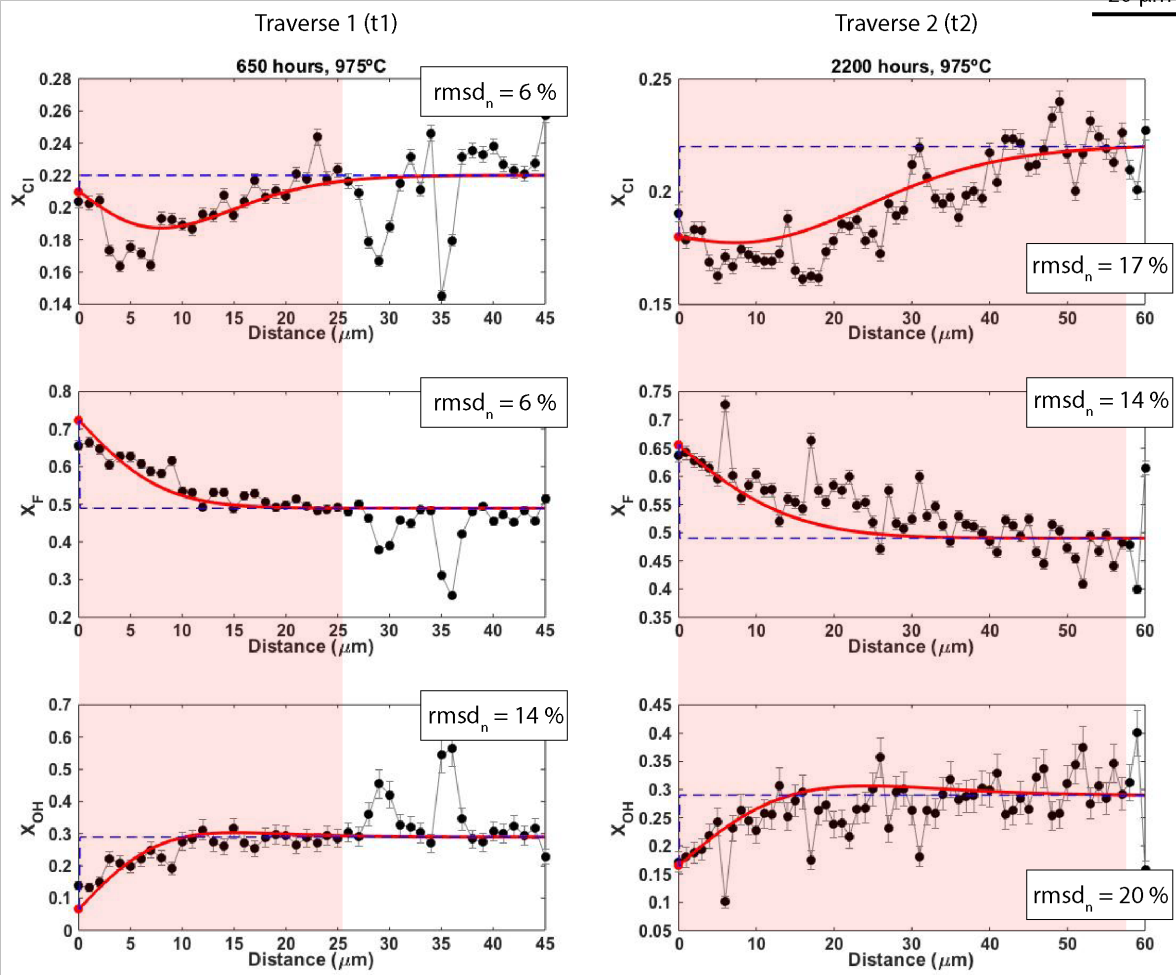
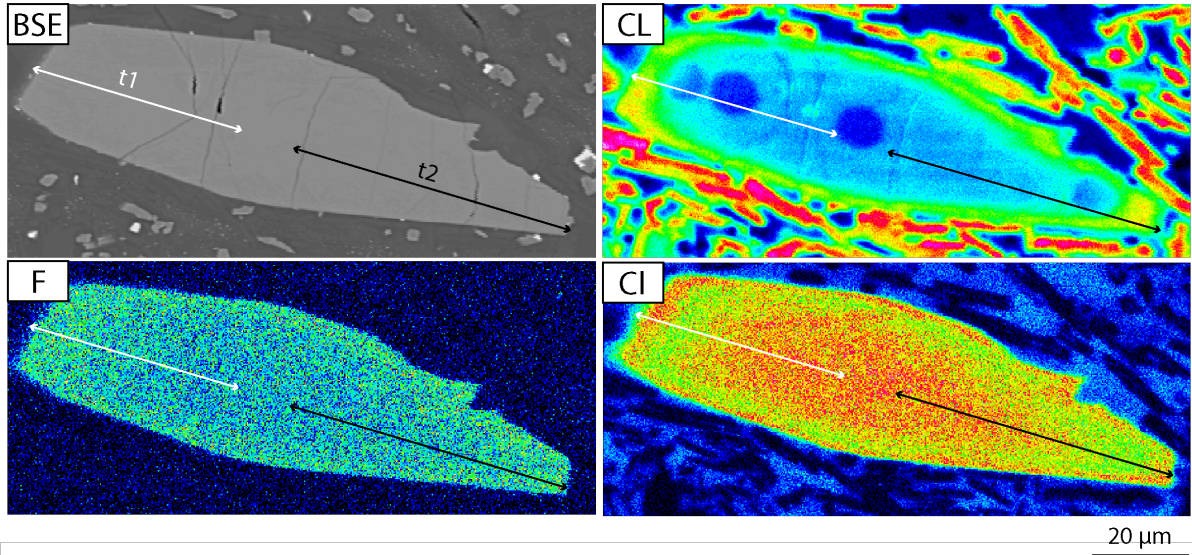


Figure S4. BSE, CL and F and Cl X-ray maps of apatite 6 in the lava flow and the associated measured profiles and best fit. The red zone corresponds to the points affected by diffusion.

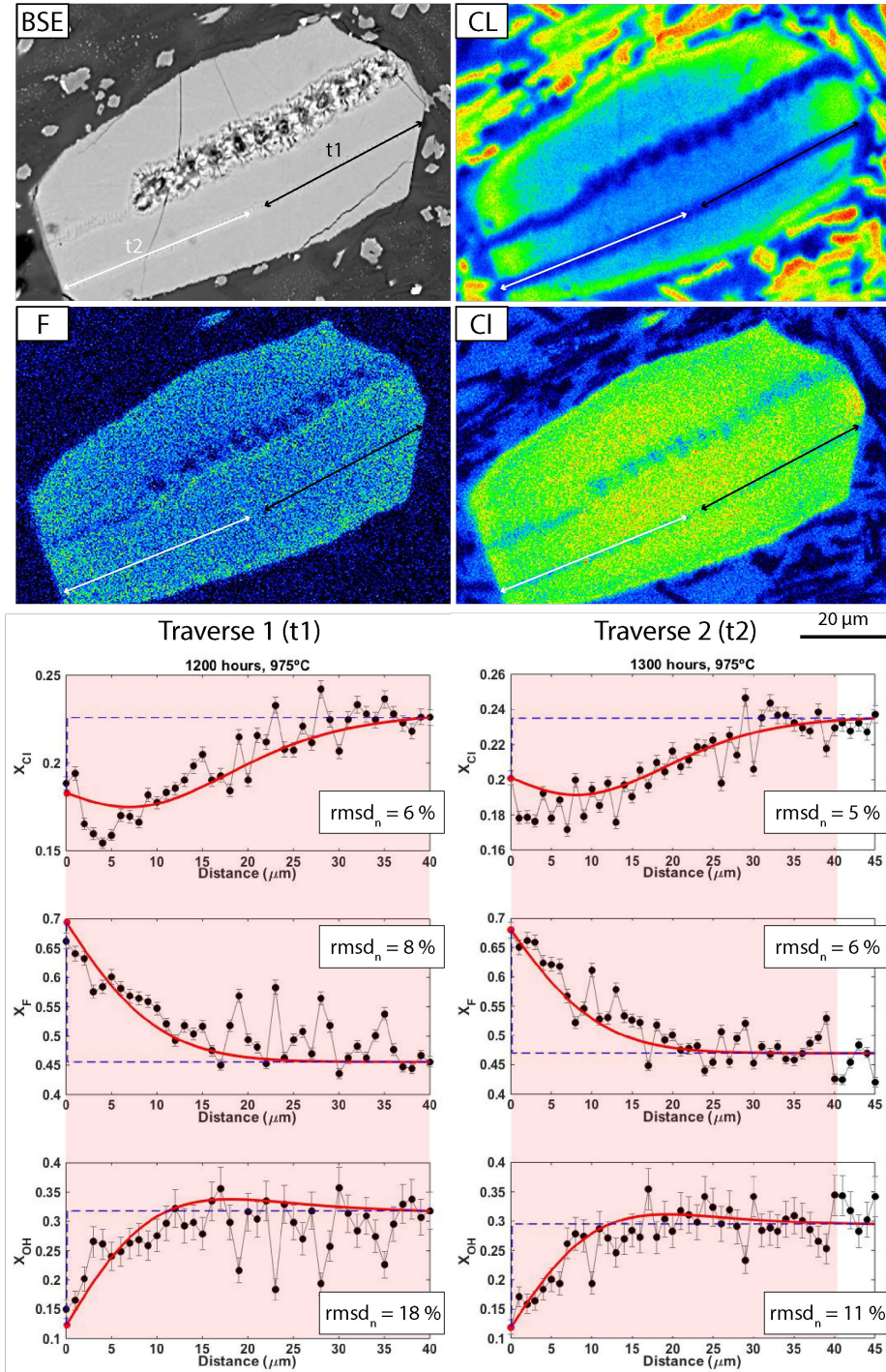


Figure S5: BSE, CL and F and CI X-ray maps of apatite 21 in the lava flow and the associated measured profiles and best fit. A first traverse was attempted which burned part of the center of the apatite due to bad coating of the thin section. The second parallel traverse that was made did not show any particular changes that could have been related to this, so we decided to use this traverse. The red zone corresponds to the points affected by diffusion.

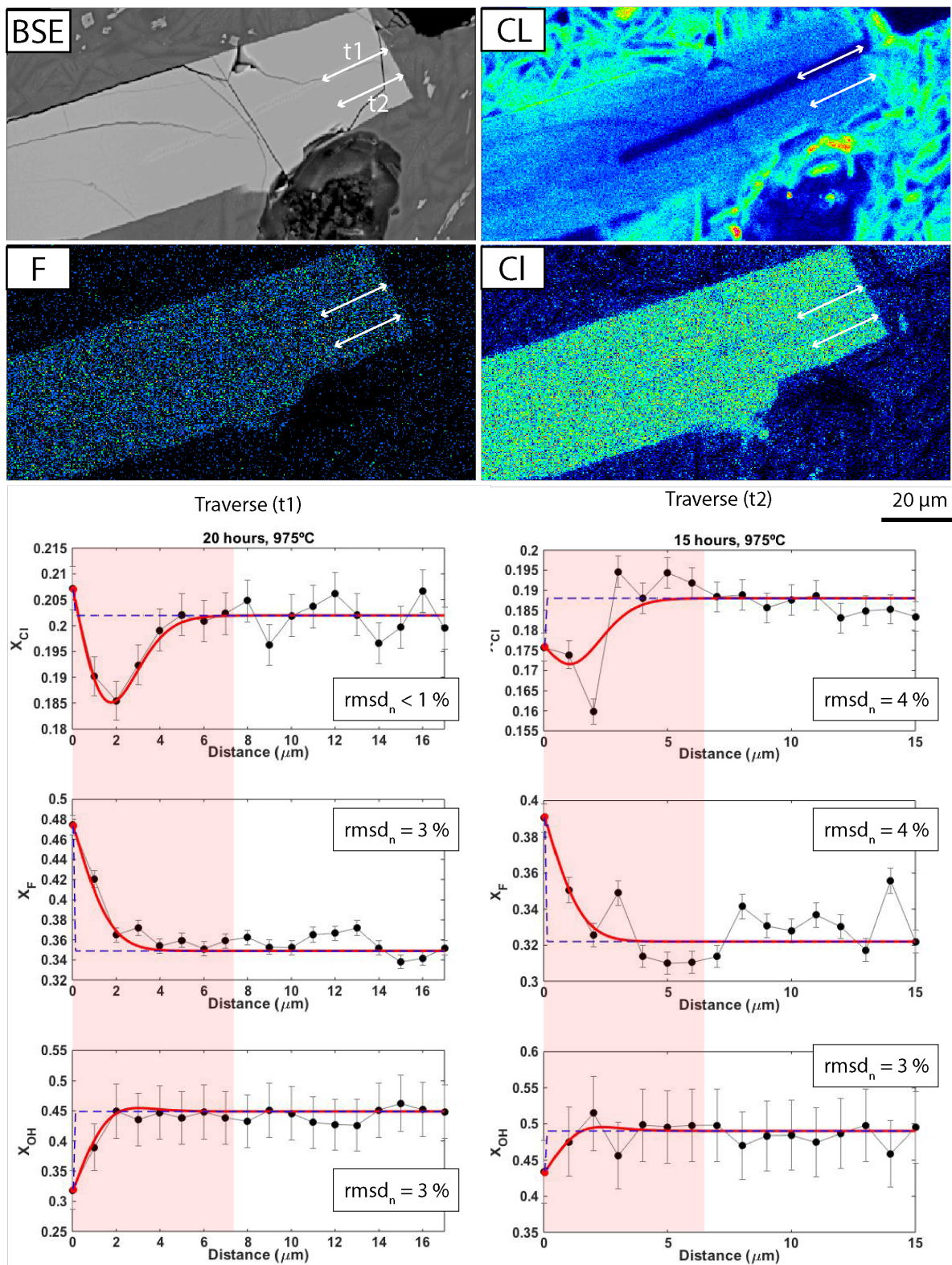


Figure S6: BSE, CL and F and Cl X-ray maps of vulcanian apatite 3 and the associated measured profiles and best fit. The red zone corresponds to the points affected by diffusion.

Vulcanian - apatite 4

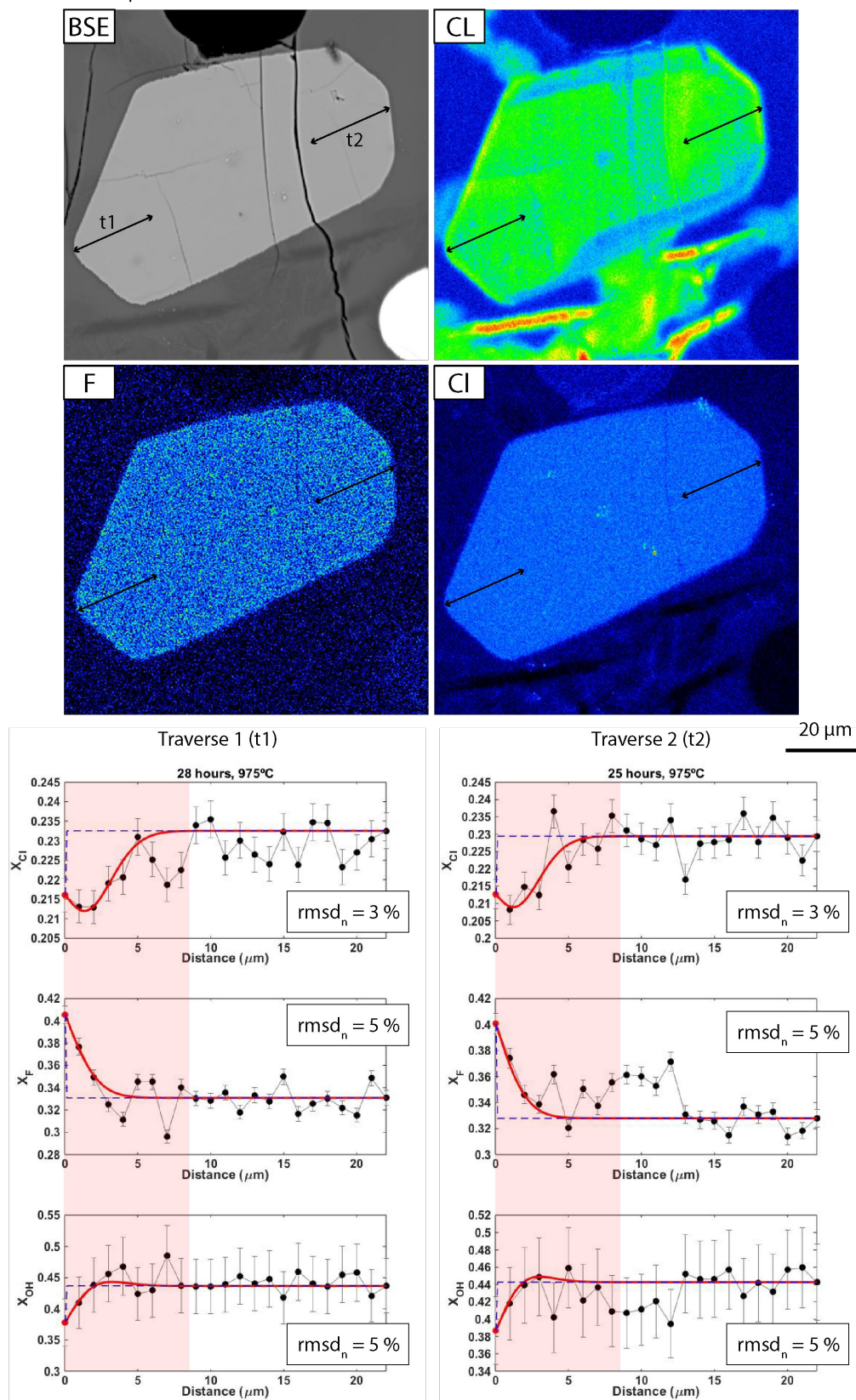
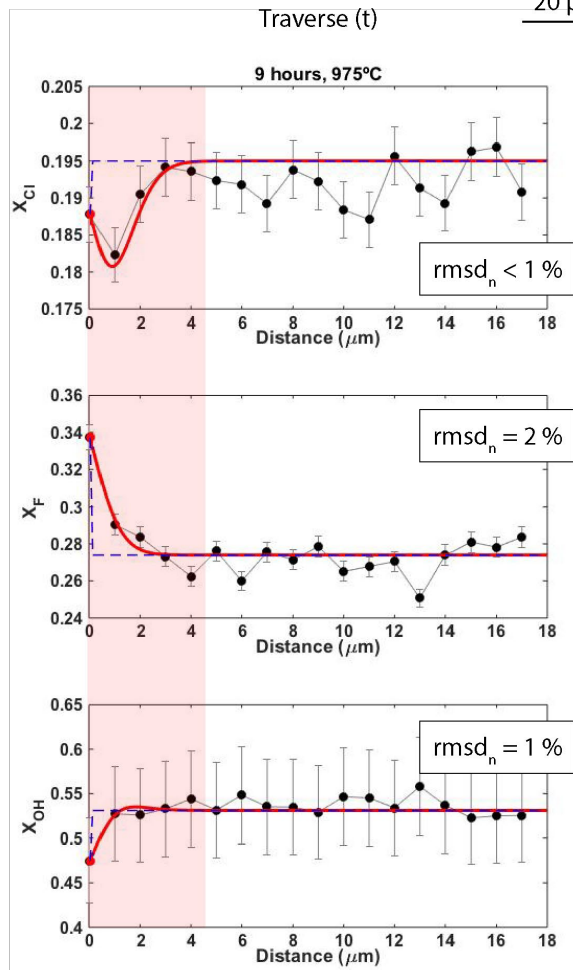
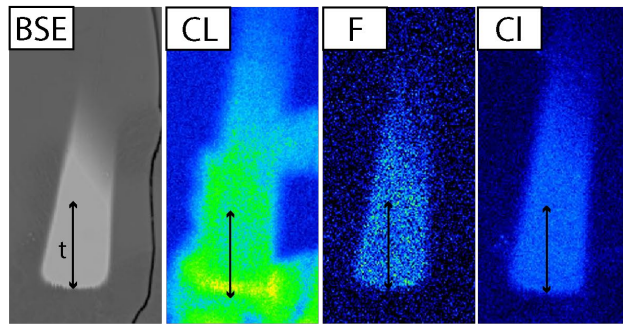


Figure S7: BSE, CL and F and Cl X-ray maps of vulcanian apatite 4 and the associated measured profiles and best fit. The red zone corresponds to the points affected by diffusion.

Vulcanian - apatite 4 bis



Vulcanian - apatite 18

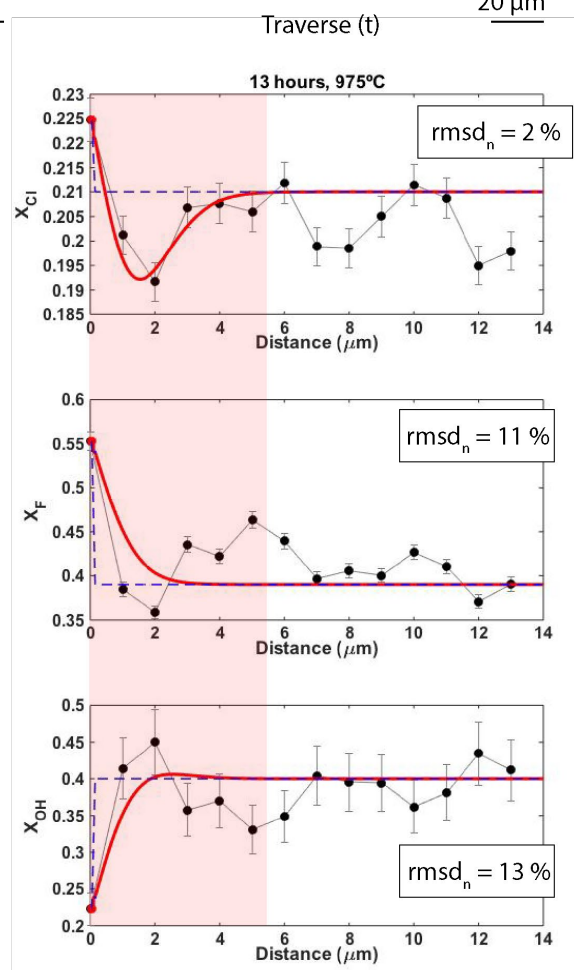
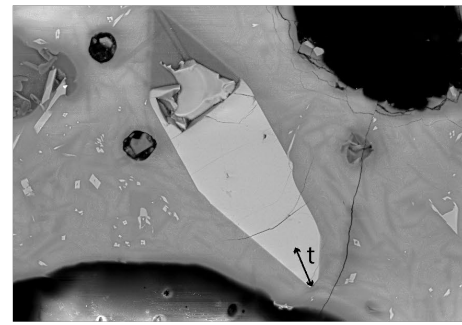


Figure S8: BSE, CL and F and CI X-ray maps of vulcanian apatite 4 bis and SEM BSE image for vulcanian apatite 18 and the associated measured profiles and best fit. No X-ray and CL images were made for apatite 18 because of lack of measuring time on the EPMA. The red zone corresponds to the points affected by diffusion.

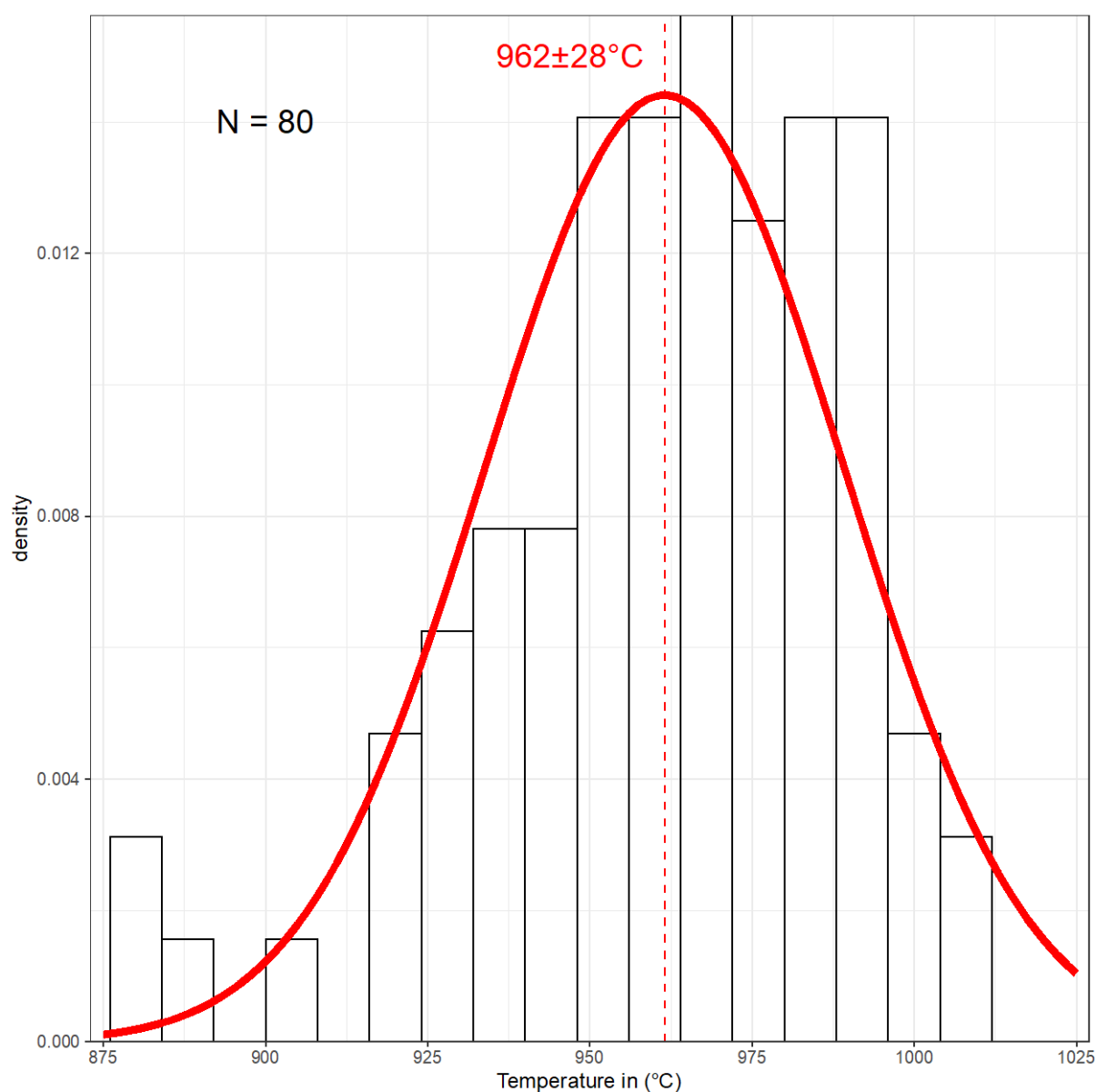


Figure S9. Apatite saturation temperatures calculated from Eq.1 of Piccoli and Candela (1994). The histogram represents apatite saturation temperatures for 80 melt compositions (melt inclusions and matrix glass). The red color curve is the modelled density curve based on the histogram. The red color text shows the average temperature and the 1-sigma standard deviation.

REFERENCES CITED

- Bernard, O., and Bouvet de Maisonneuve, C., 2020, Controls on eruption style at Rabaul, Papua New Guinea – Insights from microlites, porosity and permeability measurements: *Journal of Volcanology and Geothermal Research*, v. 406, p. 107068, doi:10.1016/j.jvolgeores.2020.107068.
- Bouvet de Maisonneuve, C., Costa, F., Patia, H., and Huber, C., 2015, Mafic magma replenishment, unrest, and eruption in a caldera setting: insights from the 2006 eruption of Rabaul (Papua New Guinea): *Geological society of London*, p. 17–39, doi:10.1144/SP422.2.
- Cherniak, D.J., 2000, Rare earth element diffusion in apatite: *Geochimica et Cosmochimica Acta*, v. 64, p. 3871–3885, doi:10.1016/S0016-7037(00)00467-1.
- Hughes, J.M., Cameron, M., and Crowley, K.D., 1991, Ordering of divalent cations in the apatite structure: Crystal structure refinements of natural Mn- and Sr-bearing apatite: *American Mineralogist*, v. 76, p. 1857–1862.
- Ketcham, R.A., 2015, Technical Note: Calculation of stoichiometry from EMP data for apatite and other phases with mixing on monovalent anion sites: *American Mineralogist*, v. 100, p. 1620–1623, doi:10.2138/am-2015-5171.
- Li, W., and Costa, F., 2020, A thermodynamic model for F-Cl-OH partitioning between silicate melts and apatite including non-ideal mixing with application to constraining melt volatile budgets: *Geochimica et Cosmochimica Acta*, v. 269, p. 203–222, doi:10.1016/j.gca.2019.10.035.
- Li, Weiran, 2019, Eruptive styles of subduction-zone volcanoes: investigation of magmatic volatile budgets and ascent rates using apatite. [Doctoral Thesis]: Nanyang Technological University, <https://hdl.handle.net/10356/84205>.